Robotica (2022), **40**, pp. 3435–3462
doi:10.1017/S0263574722000327

CAMBRIDGE UNIVERSITY PRESS

RESEARCH ARTICLE

Compliance modeling of a full 6-DOF series–parallel flexure-based Stewart platform-like micromanipulator

Suraj Kumar Mishra* and Cheruvu Siva Kumar

Robotics and Intelligent Systems Laboratory, Department of Mechanical Engineering, Indian Institute of Technology, Kharagpur, India
*Corresponding author. E-mail: surajkmishra@iitkgp.ac.in; surajkmishra1989@gmail.com

Received: 22 October 2021; **Revised:** 1 January 2022; **Accepted:** 16 February 2022; **First published online:** 22 March 2022

Keywords: Stewart platform, compliant parallel micromanipulator, compliance modeling, stiffness modeling, matrix method, FEA

Abstract

With many micromanipulator designs emerging in micro and nanosystem applications, the element of compliance in the mechanisms is gaining attention. Several designs consider motions limited in a plane for high accuracy and repeatability as needed in micro/nano manipulation applications. Extending this to a full spatial configuration with coupled motions of series and parallel linkages with flexure joints of 1-degree-of-freedom (DOF) and 3-DOF needs a systematic analytical approach. One such approach for compliance analysis is presented in this article for a mechanism designed at Indian Institute of Technology Kharagpur. To validate the analytical models, finite element analysis simulations are performed with the help of the Abaqus-6.14 software package. Following the successful validation, the effect of structural parameters on the performance is presented with the help of the analytical expressions. We explore the performance of the mechanism with different dimensions of flexures of a particular type. Results indicate that the design with dissimilar dimensional parameters can give superior performance.

1. Introduction

With several recent developments in nanotechnology, there is considerable interest in exploring, manipulating, assembling, and fabrication of structures and systems at the micro and nanoscales. Nowadays, micromanipulators are being used for manipulation and motion generation in microscale environments such as in optical microscopes, electron microscopes and applications wherein 2D/3D micromanipulation of materials is carried out.

In the case of robotic manipulation, compliance is generally perceived as an undesirable but unavoidable characteristic. The external loading and self-weight lead to a nonnegligible deflection of the end effector. This deflection affects the accuracy of the operation and degrades the quality of the final product. While this is true for a large scale, high payload, and high range manipulation, there are situations wherein the external loads are extremely low, required motion is in micro/nano scales, and accuracy is of paramount importance. A flexure-based compliant mechanism such as the one discussed in this article is highly suitable in this context. Compliant mechanisms are a category of mechanisms that involve the deformation of some of its joints or members for creating movements [1]. This particular class of mechanisms purposefully incorporates compliance into the system to exploit certain benefits. For instance, the compliant flexure joints eliminate backlash and friction, thus, offering better accuracy. Furthermore, the low weight of these mechanisms ensures that they have negligible deformation/deflection due to self-weight. The flexure-based compliant mechanism has a limitation on the range of motion. However, as the required motions are in micro/nano scales, this shortcoming practically does not matter. To sum up, for specific applications involving low payload, precision micromanipulation, the benefits of inclusion of compliance outweigh its limitations; consequently, flexure-based compliant mechanisms are widely

employed in such cases. Compliant mechanisms at microscales are increasingly being used for precise actuation or motion/force sensing mechanisms in micro electro mechanical systems.

Compliant mechanisms with serial structure offer large workspace and dexterous maneuverability, but as they have cantilever structures, they are more prone to deform/deflect under loading. Moreover, the serial arrangement of members leads to the accumulation of errors. In addition, at high speeds, vibration becomes a severe challenge in serial structured mechanisms. All these reasons make serial structure unsuitable for fast and precise micromanipulation. To conquer the limitations of serial structures, parallel structures have drawn extensive attention. Here, several independently actuated links connect the end effector to the base. The parallel structure ensures improved rigidity and higher load-carrying capacity. Moreover, this arrangement avoids error accumulation providing better positioning. Therefore, it can be concluded that a compliant mechanism with a parallel kinematic structure is the most preferred solution for micro-motion applications. These types of mechanisms are popularly known as compliant parallel micromanipulators (CPMs).

In the design process of a CPM, compliance analysis or stiffness analysis plays a significant role [2–4]. Analytical compliance modeling allows us to observe the effect of structural parameters of the CPM on performance. It also helps us to understand the static, modal, and dynamic behavior of the system whereby it is possible to provide in the design of a CPM with high stiffness that leads to higher natural frequency, good repeatability, dexterous, and precise manipulation [2].

A coverage of different methods of compliance modeling can be found in the work of Ling et al. [5]. The finite element analysis (FEA) has been often used to do compliance modeling and is considered most accurate. Alternatively, researchers use pseudo-rigid body (PRB) modeling [6–9]. However, since the PRB model considers the compliance of the members in their working or on-axis direction only, it is not much useful for complete compliance analysis of a spatial mechanism. This method is mostly used for CPM with simpler designs or in cases where undesired or out of axis deformations are very low or negligible. A highly accurate analytical model can be formulated by considering the full nonlinear model of all the members of the mechanism [10, 11]. Unfortunately, such models become too involved for a spatial CPM with a large number of members. Further, the nonlinear method does not offer much benefit for a system undergoing small deformations. Therefore, it is suitable only where the system is subjected to large deformations like that of a compliant mechanism with distributed compliance. In the present context, with consideration of 6D compliance, a lumped parameter model of the members can be used as a compromise [2, 12, 13]. With the assumption of Hooke's law, this lumped model can be formulated very easily by using the matrix method.

Although an extensive amount of research has already been done in the area of compliance or stiffness analysis [3, 4, 14–17], most of these study deal with the case of planar mechanisms or in applications involving planar motions. There is not much work available for spatial mechanisms having multiple degree-of-freedom (DOF). Some of the other recently reported works can be seen in refs. [18–22].

In a previous work of the authors, a compliant Stewart platform-based micromanipulator for high range 6-DOF motion applications was proposed [23]. It was shown that for its size, the design gives a better range of motion than other similar CPMs. The model has a full 6-DOF spatial motion capability that is achieved using six separate parallelogram linkages. The kinematic structure of these linkages so arranged offers a unique 6-DOF motion similar to that of a Stewart platform but at micro and nanoscales. However, carrying out a full compliance model of such a micromanipulator is not an easy task. The parallel paths of compliances in the combination of rigid and flexure linkages used along with a spatial disposition of each member needs a systematic process to build accurate models. In such a case, we consider a model for full 6-DOF motion with lumped compliance parameters in our paper.

The matrix method is used to derive the expressions for output compliance and input compliance. The proposed CPM takes into consideration parallelogram linkages in each limb to achieve a higher range of motions in a plane. The analytical expression for the amplification ratio (AR) for such parallelogram linkages has been derived in the article. Since the behavior of a compliant mechanism greatly

https://doi.org/10.1017/S0263574722000327 Published online by Cambridge University Press

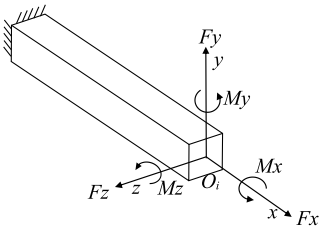

Figure 1. *A flexure member subjected to a general force vector at its free end.*

depends on the compliance of the flexures incorporated in the design, factors like the type of joints, its geometrical parameters, and material are considered. In this article, we consider the spatial mechanism with two classes or types of flexure joints; and we allow different geometrical parameter for one of the types/classes. This is an important consideration in spatial CPM as compared to planar CPM that often assumes the same geometric features at flexure joints mostly due to manufacturing considerations. We determine the advantage of providing varied geometry and compliance in one type of flexure joints on the performance of the spatial mechanism.

The contributions of this article are as follows. We present a thorough approach to an analytical compliance analysis of a spatial 6-DOF micromanipulator, which has not been addressed much in the literature. For a spatial 6-DOF micromanipulator, the compliances are interwoven with the geometry of motion and the derivation of expression needs a systematic approach to represent the effective spatial compliance matrix. This procedure is highlighted and customized for a specific design of a system developed at Indian Institute of Technology (IIT) Kharagpur. The article also presents a procedure to obtain the analytical expression for the AR in terms of the compliance factors. The analytical expression of the AR is significant as it allows the designer to achieve a better amplification of motion by changing flexures' geometry. Moreover, the availability of the analytical relations allows a designer to optimize the CPM's geometry for the desired behavior. In most of the available work, authors do not consider the connecting links' compliance and assume them as rigid members in their models. In our work, we have also incorporated the compliance of the connecting links along with that of the joints and have shown that the geometry of the connecting links has a significant effect on amplification of motion indeed. This is needed to access the cross-coupled effects of both joints and linkages in the distributed compliance system in all 6-DOF. Finally, the work establishes that the provision of flexures with different geometrical parameters can improve performance.

The organization of the rest of the article is as follows: In Section 2, the methodology used for compliance modeling has been discussed. A representation to define and to carry out transformation in the spatial domain is presented. Section 3 outlines the design of the micromanipulator briefly. The analytical model of output compliance, input compliance, and AR has been derived in Section 4. Validation of the derived mathematical model has been done in Section 5 with the help of Abaqus-6.14 simulation. Based on the analytical models, Section 6 presents the effect of dimensional parameters on the performance of the CPM. This section also presents the effects of dissimilar geometry. In the end, concluding remarks have been summarized in Section 7.

2. Compliance modeling of a CPM based on matrix method

Compliance modeling is carried out using the concept of a compliance matrix. For any flexure or compliant member, it can be shown that a compliance matrix maps the force vector and the displacement vector. Figure 1 shows a typical member in its frame *i* subjected to a generalized force at its end.

https://doi.org/10.1017/S0263574722000327 Published online by Cambridge University Press

The 6 × 6 local compliance matrix for this member can be represented as

$$C_i = \begin{bmatrix} C_{xFx} & 0 & 0 & 0 & 0 & 0 \\ 0 & C_{yFy} & 0 & 0 & 0 & C_{yMz} \\ 0 & 0 & C_{zFz} & 0 & C_{zMy} & 0 \\ 0 & 0 & 0 & C_{\theta xMx} & 0 & 0 \\ 0 & 0 & C_{\theta yFz} & 0 & C_{\theta yMy} & 0 \\ 0 & C_{\theta zFy} & 0 & 0 & 0 & C_{\theta zMz} \end{bmatrix} \tag{1}$$

where compliance factor C_{xFx} represents the displacement in x-direction due to a unit force in x-direction. Whereas C_{yMz} denotes the displacement in y-direction due to a unit moment Mz about z-axis. The other members of the matrix can be defined in a similar manner. The compliance factors for different types of flexures have been formulated in several refs. [24–26].

In Eq. (1), C_i denotes the local compliance at O_i. The absence of superscript in C_i means that the compliance is defined with respect to the fixed end or ground. Now, to transfer this compliance into any other coordinate system, let us say O_j, we can use the following expression as described in ref. [12]

$$C_j = T_i^j C_i \left(T_i^j\right)^T \tag{2}$$

where transformation matrix T_i^j is defined as

$$T_i^j = \begin{bmatrix} R_i^j & S\left(r_i^j\right) R_i^j \\ 0 & R_i^j \end{bmatrix} \tag{3}$$

where R_i^j is a rotation matrix which represents orientation of coordinate system O_i with respect to O_j, r_i^j represents the position vector of the point O_i with respect to O_j. $S(r)$ is the skew-symmetric matrix, and for a position vector: $r = [r_x \;\; r_y \;\; r_z]$, it has the following form

$$S(r) = \begin{bmatrix} 0 & -r_z & r_y \\ r_z & 0 & -r_x \\ -r_y & r_x & 0 \end{bmatrix} \tag{4}$$

A flexure-based CPM may have members connected in a serial, a parallel, or in a compounded series–parallel configuration. The procedure to derive the compliance equation of a generalized system is presented in the following section.

2.1. Procedure for obtaining output compliance, input compliance, and amplification ratio for a generalized CPM with series–parallel configuration

This section discusses the procedures to formulate analytical models for output compliance, input compliance, and AR for a general CPM. The outlined methods can easily be applied to the other designs. Let us consider a typical simplified CPM as shown in Fig. 2. The CPM has N-limbs ($S_1, S_2, \ldots, S_N$) with m number of flexure members. The limb S_1 comprises of a serial chain of joints and links; S_2 comprises of series of sub chains SS_1 and SS_2; SS_1 is a parallel chain of joints and linkages; SS_2 and SS_1 are in series. The combined $S_1, S_2, .., S_N$ are all in parallel chain configuration. Limb-S_N incorporates a motion amplification system wherein F is the input point and D is the output point.

2.1.1. Output compliance

The output compliance of this mechanism is the compliance of the whole system at output point O. Firstly, we should determine the compliance of each of the limbs. In the first limb S_1, flexure-1 and flexure-2 are in series, so their compliances can be added after transforming them to point A.

$$C_A = T_1^A C_1 \left(T_1^A\right)^T + T_2^A C_2 \left(T_2^A\right)^T \tag{5}$$

https://doi.org/10.1017/S0263574722000327 Published online by Cambridge University Press

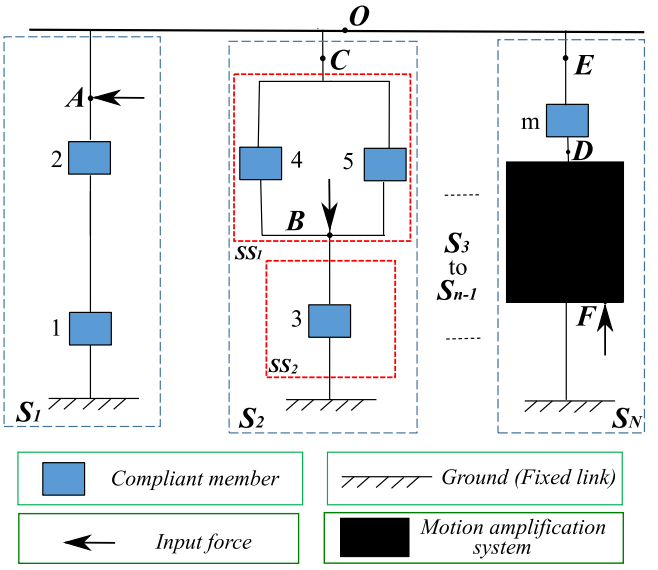

Figure 2. *Schematic diagram of a generalized compliant parallel manipulator.*

The limb-S_2 itself has a combination of series and parallel connections, therefore, it is further divided into subsystems SS_1 and SS_2. Compliance of subsystem SS_2 at B is

$$C_{B:SS_2} = C_B = T_3^B C_3 \left(T_3^B\right)^T \tag{6}$$

The subsystem SS_1 contains flexure-4 and flexure-5 in parallel. These compliances will first be transformed to the point C, and then, the inverse of these transformed compliances will be added. The desired compliance of the subsystem will be the inverse of the obtained sum. The equation for this process is presented below.

$$C_{C:SS_1}^B = C_C^B = \left(\left(T_4^C C_4 \left(T_4^C\right)^T\right)^{-1} + \left(T_5^C C_5 \left(T_5^C\right)^T\right)^{-1}\right)^{-1} \tag{7}$$

The superscript B in the notation here indicates that point B is considered the reference or fixed point.

Subsystems SS_1 and SS_2 are in a serial chain. Therefore, the total compliance of the limb-S_2 at C can be obtained by adding the transformed compliances of SS_1 and SS_2 as given below.

$$C_C = T_B^C C_B \left(T_B^C\right)^T + C_C^B \tag{8}$$

This process will be done for each of the limbs. Finally, the compliance for the last limb-S_N at point E is

$$C_E = T_m^E C_m \left(T_m^E\right)^T + T_D^E C_D \left(T_D^E\right)^T \tag{9}$$

We have determined the compliance of all the limbs at their output points. Since all the limbs are in parallel, the output compliance of the full mechanism at O can be obtained by the following equation as done earlier.

$$C_O = \left(\left(T_A^O C_A \left(T_A^O\right)^T\right)^{-1} + \left(T_C^O C_C \left(T_C^O\right)^T\right)^{-1} + \ldots.. + \left(T_E^O C_E \left(T_E^O\right)^T\right)^{-1}\right)^{-1} \tag{10}$$

2.1.2. Input compliance

Input compliance is defined as the compliance of the actuated (or input) point of the CPM. If the CPM has a symmetric design, all the actuated points would yield identical input compliance. However, an

https://doi.org/10.1017/S0263574722000327 Published online by Cambridge University Press

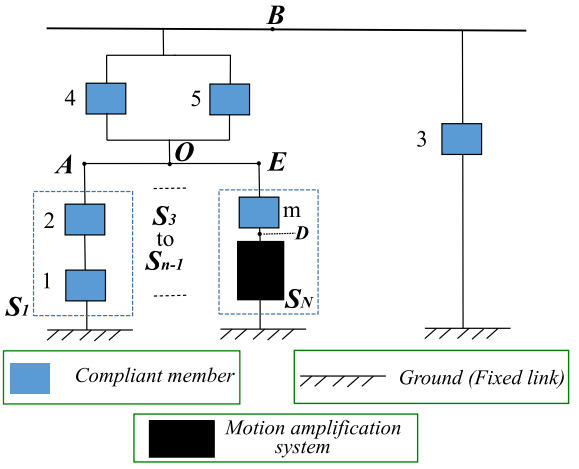

Figure 3. *Schematic diagram of the modified CPM for input compliance determination.*

asymmetric CPM may provide different values of input compliance. The generalized CPM in consideration here has an asymmetric design. In what follows, we shall try to determine one of the input compliances. The other input compliances can be obtained using a similar procedure.

Let us consider the input point B (Fig. 2) in limb-S_2 for input compliance determination. The next step is to rearrange the system to make B the output point. Figure 3 shows the modified system after such rearrangement. The desired compliance is nothing but the output compliance of this modified system, which can be obtained by following the process discussed in the last section.

2.1.3. Amplification ratio or displacement amplification

The current generalized CPM contains a motion amplifier in the limb S_N (Fig. 2). The AR for this system would be the ratio of displacement of its output point D to that of input point F. The determination of the AR typically involves the following steps.

1. Isolate the motion amplification system from the full mechanism as shown in Fig. 4.
2. Consider the mechanism left after removing the amplification system (Fig. 4a), and write force–displacement/(moment–rotation) equations at the bifurcation point (D).
3. Write force–displacement/(moment-rotation) equations for the separated amplification system (Fig. 4b) at input point F and point D.
4. Solve the algebraic equations generated from Step (2) and Step (3) to formulate the expression for AR.

3. Design of the 6-DOF flexure-based stewart platform-like CPM

Before carrying out the compliance analysis of the micromanipulator in consideration, we shall briefly discuss its design. The design of the mechanism is based on the Stewart platform [27, 28]. A compliant version of the mechanism developed at IIT Kharagpur is being considered [23]. In the design, right circular revolute and right circular spherical flexures (Figs. 5a and 5b, respectively) have been utilized in each limb of the mechanism. As mentioned earlier, the current design has a provision of parallelogram linkages in each limb. The kinematic diagram for a limb in Fig. 6 shows the locations wherein the flexure joints will be placed.

Figure 7 presents a detailed engineering description of the limb with flexure joints of the micromanipulator designed at IIT Kharagpur. All the revolute flexures in the parallelogram mechanism have been

https://doi.org/10.1017/S0263574722000327 Published online by Cambridge University Press

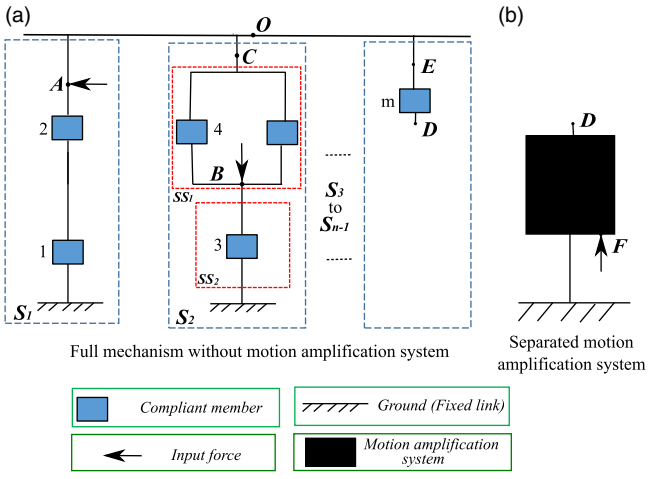

Figure 4. *Schematic diagram for amplification ratio determination.*

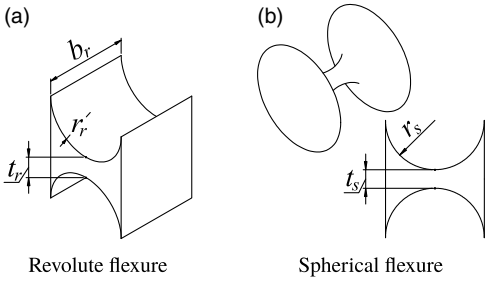

Figure 5. *Design elements of the micromanipulator.*

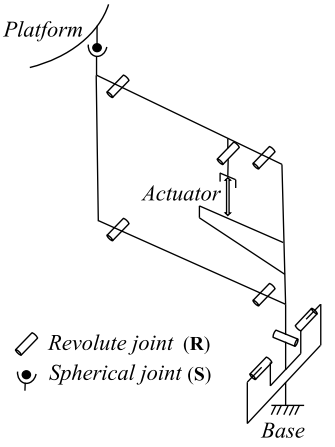

Figure 6. *Kinematic diagram of a limb of the mechanism.*

provided with identical dimensions. The full design of the Stewart CPM involves six limbs connected in a parallel configuration as shown in Fig. 8(b), which mimics the 6-DOF Stewart platform shown in Fig. 8(a). Figure 9 presents two views of the micromanipulator wherein the top view shows the relative description of the links and the side view/elevation is shown to represent the effect of motion/loads used in compliance analysis.

https://doi.org/10.1017/S0263574722000327 Published online by Cambridge University Press

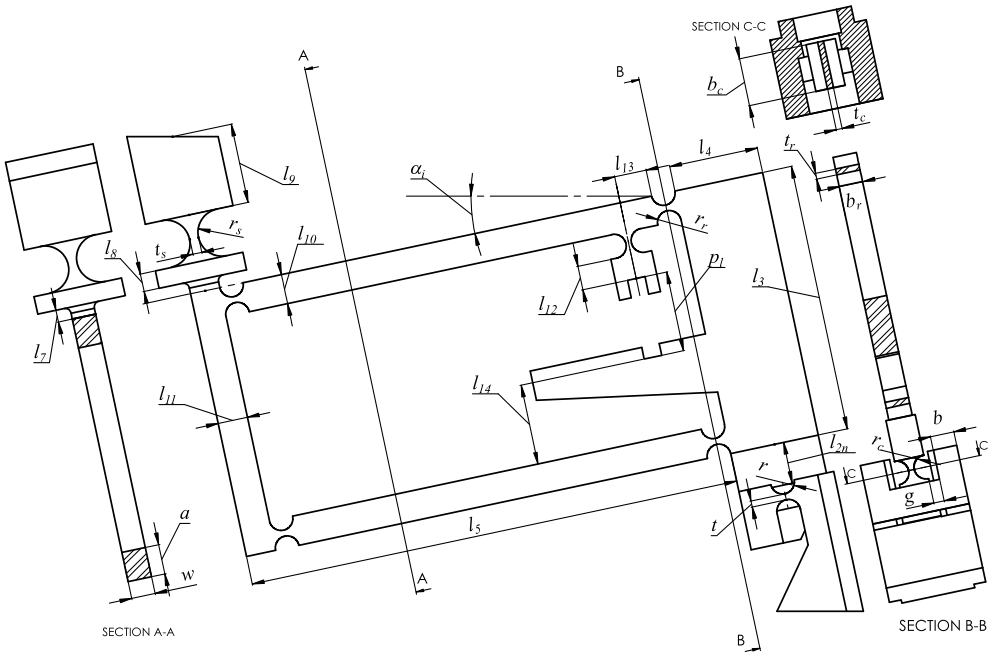

Figure 7. *A limb of the micromanipulator with dimensions.*

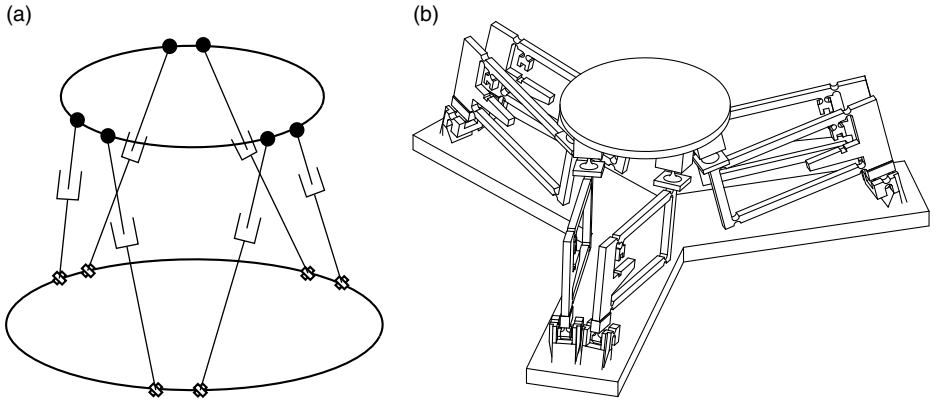

Figure 8. *The general Stewart platform and compliant version of the micromanipulator.*

4. Full 6-DOF spatial compliance modeling of the flexure-based stewart platform-like CPM

As per the objective of this work, for our micromanipulator, consider the following in our study: (a) output compliance of the entire mechanism, (b) input compliance at an input point of a limb, and (c) AR of the parallelogram linkage for a limb.

Output compliance of the present CPM can be defined as the motion of the end-effector point *M* (Fig. 9) when a unit external load is applied at the same point [29]. As per the compliance matrix defined in Eq. (1), output compliance has many components or factors. These factors describe the force/moment–displacement/rotation behavior of the CPM at the output point. The output compliance plays a very crucial role for accurate manipulation when the end effector is subjected to an external force or loading.

https://doi.org/10.1017/S0263574722000327 Published online by Cambridge University Press

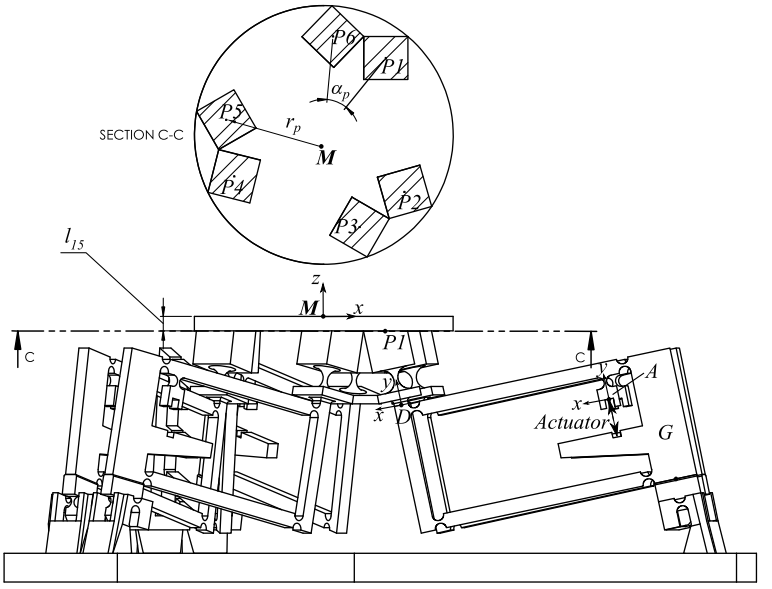

Figure 9. *Output compliance, input compliance, and amplification ratio.*

A CPM with low output compliance (or high output stiffness) can perform its motion with precision without being influenced by external loads.

Input compliance for a CPM relates the input force and the resulting input motion [30]. For the given Stewart platform-based CPM, input compliance is the compliance of input point A in y-direction with respect to link G of the parallelogram mechanism of the limb (Fig. 9). For safe operation, this input compliance should be more than the output compliance of the actuator.

The AR for the parallelogram linkage is defined as the ratio of output motion (motion of point D in y-direction in its local coordinate frame) to the input motion (motion of point A in y-direction in its local coordinate frame) of the parallelogram mechanism of the limb (Fig. 9). Again, the input and output motions are defined with respect to the link G, which is the actuator's reference link. The compliance or stiffness of the actuators is not considered in the present study. The analytical expressions for compliances are generated by symbolic computation software Maple-18 [31], as these expressions can get cumbersome.

4.1. Modeling of output compliance

There are three different types of compliant members used in the design of the CPM in consideration: revolute flexures, spherical flexures, and deformable connecting links (modelled as Euler−Bernoulli beams as applicable). In compliance modeling, each of these members needs to be assigned coordinate frames. Figure 10 illustrates the scheme of coordinate system assignment followed in this article.

With reference to Fig. 9, we can observe that the micromanipulator consists of six similar limbs with parallelogram linkages connected in a parallel configuration. In what follows, the expression of output compliance for one of the limbs will be derived.

4.1.1. Modeling the output compliance of a single limb

Referring to Fig. 7, it may be noted that the design of the limb involves several compliant members. For easier identification of these members, the key nodes and points are assigned numbers, as shown in Fig. 11. These comprise one of the three elements described in Fig. 10. The flexible members are shown in the legend table of Fig. 11; all other members in the system are considered as rigid. It can be seen

https://doi.org/10.1017/S0263574722000327 Published online by Cambridge University Press

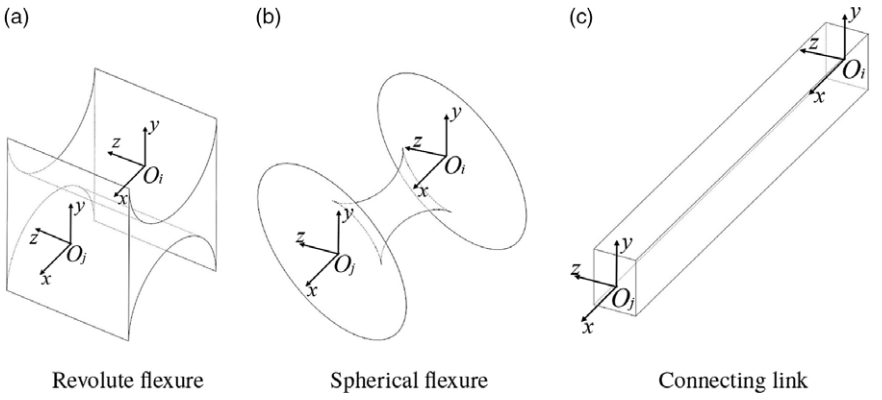

Figure 10. *Coordinate system assignment scheme for compliant members.*

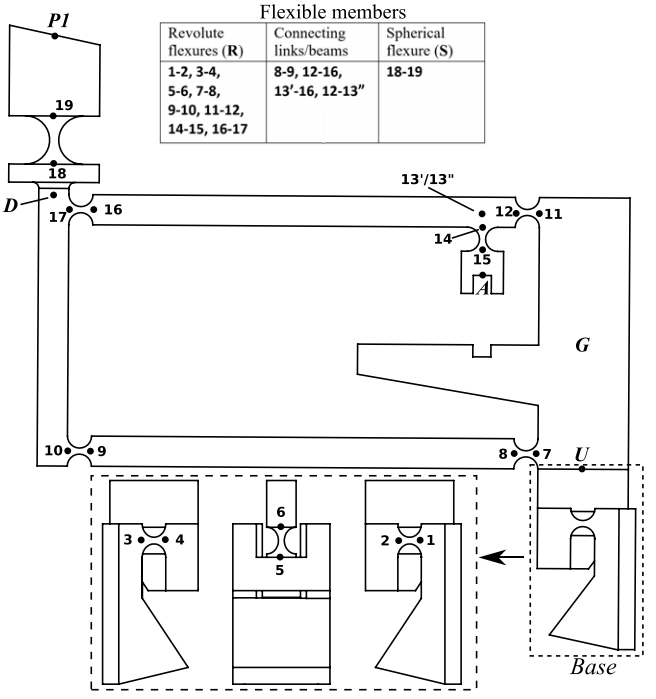

Figure 11. *Numbering of key nodes and points in the limb-1 of the mechanism.*

that every member has been assigned two nodes. Out of these two nodes, one would be the output node based on how we proceed in the micromanipulator design for a particular calculation. The compliant member will be referred by this output node.

For the sake of convenience, a limb of the micromanipulator can further be divided into three subsystems (Fig. 11): (i) compliant universal joint (From base to *U*), (ii) compliant parallelogram mechanism (From *U* to *D*), and (iii) compliant spherical joint (from *D* to *P*1). The connectivity graph of all the members in the limb has been depicted in Fig. 12.

The first subsystem is the universal joint. It is constructed by the combination of three revolute flexures (joint-2, joint-4, and joint-6). For the universal joint, we can see that joint-2 and joint-4 are in parallel connection, and their end is in serial connection with joint-6 (Fig. 12). Hence, the compliance of the

https://doi.org/10.1017/S0263574722000327 Published online by Cambridge University Press

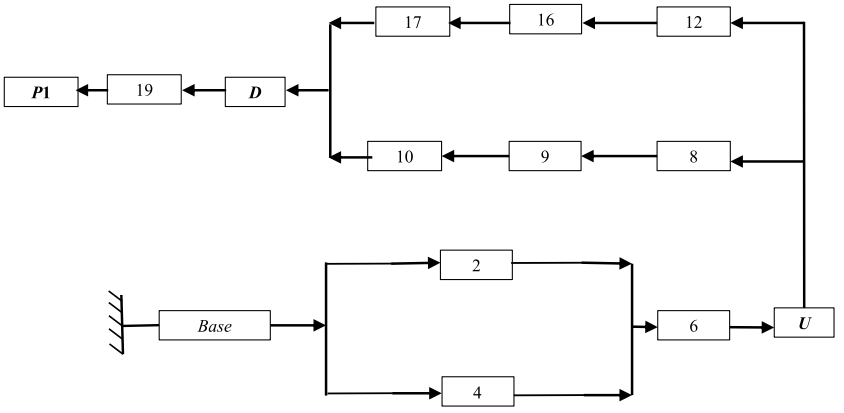

Figure 12. *Connectivity graph of members in a limb for output compliance determination.*

universal joint at point U can be written as

$$C_u = \left(\left(T_2^u C_2 \left(T_2^u \right)^T \right)^{-1} + \left(T_4^u C_4 \left(T_4^u \right)^T \right)^{-1} \right)^{-1} + T_6^u C_6 \left(T_6^u \right)^T \tag{11}$$

where C_2, C_4, and C_6 are the compliance matrices for revolute flexure, and T_2^u, T_4^u, and T_6^u are corresponding transformation matrices. The detailed description of all the transformation and compliance matrices used in this article can be found in the appendices. The second subsystem is the parallelogram mechanism. Considering the series and parallel connection of different members (Fig. 12), the compliance of point D with respect to point U can be expressed as

$$C_D^U = \left(\left(T_8^D C_8 \left(T_8^D \right)^T + T_9^D C_9 \left(T_9^D \right)^T + T_{10}^D C_{10} \left(T_{10}^D \right)^T \right)^{-1} + \left(T_{12}^D C_{12} \left(T_{12}^D \right)^T \right. \right.$$
$$\left. \left. + T_{16}^D C_{16} \left(T_{16}^D \right)^T + T_{17}^D C_{17} \left(T_{17}^D \right)^T \right)^{-1} \right)^{-1} \tag{12}$$

The third and final subsystem is the compliant spherical joint. For this joint, compliance at $P1$ with respect to point D is

$$C_{P1}^D = T_{19}^{P1} C_{19} \left(T_{19}^{P1} \right)^T \tag{13}$$

where C_{19} is the compliance matrix for spherical flexure joint. For the current design of the compliant spherical flexure, errors in the analytical relations (from ref. [25]) were very high; hence for this flexure values of compliance factors has been taken from FEA simulations.

Figure 11 shows that the universal joint, parallelogram linkage, and spherical joint are serially connected. Therefore, from Eqs. (11) to (13), the final expression of compliance for full limb at $P1$ (with respect to ground) is

$$C_{P1} = T_u^{P1} C_u \left(T_u^{P1} \right)^T + T_D^{P1} C_D^U \left(T_D^{P1} \right)^T + C_{P1}^D \tag{14}$$

The expression of output compliance for other five limbs can be formulated by following similar procedure.

4.1.2. Output compliance of the full model

The full compliant model of the current CPM is composed of six limbs connected in the parallel configuration, as shown in Fig. 9. Firstly, to derive the output compliance, the local compliances of these limbs will be transformed to the global coordinate frame M. Then, taking into account their parallel

https://doi.org/10.1017/S0263574722000327 Published online by Cambridge University Press

connection, the final output compliance at M can be expressed as

$$C_M = \left(\left(T^M_{P1} C_{P1} \left(T^M_{P1}\right)^T\right)^{-1} + \left(T^M_{P2} C_{P2} \left(T^M_{P2}\right)^T\right)^{-1} + \left(T^M_{P3} C_{P3} \left(T^M_{P3}\right)^T\right)^{-1} + \left(T^M_{P4} C_{P4} \left(T^M_{P4}\right)^T\right)^{-1} + \left(T^M_{P5} C_{P5} \left(T^M_{P5}\right)^T\right)^{-1} + \left(T^M_{P6} C_{P6} \left(T^M_{P6}\right)^T\right)^{-1}\right)^{-1} \tag{15}$$

Above is the equation for output compliance of the full micromanipulator.

4.2. Amplification ratio and input compliance

The provision of motion amplifier is common in flexure-based micromanipulators. The motion amplification in a compliant micromanipulator depends not only on its kinematics but also on the compliances of the members in it. Therefore, an analytical analysis in present context becomes essential as it can give the designer insights on the influence of design parameters on amplification. The analytical model can also be employed to optimize the geometry of mechanism for obtaining maximum possible amplification.

As defined before, the AR is the ratio of output motion to the input motion in the parallelogram mechanism of a limb. To formulate the expression for AR, the parallelogram mechanism of one of the limbs needs to be separated from the full mechanism. It should be noted that the input and output motions are defined with respect to the link G, and they do not involve the rigid-body motions of the parallelogram mechanism. Therefore, for the determination of input and output motion, the link G is assumed to be fixed in the present case. Figure 13(a) shows the separated parallelogram mechanism of limb-1 with suitable reactions. This separated mechanism will be referred to as parallelogram-1. Out of all six actuator locations, if actuation is only taking place at parallelogram-1, then the reaction forces at point D on the parallelogram-1 can be assumed to be in the plane of the mechanism. Even if any out-of-plane reaction forces occur, they will have a negligible effect on the amplification process of the mechanism. Moreover, since point D is situated at the output of the parallelogram mechanism, its planar rotation can be assumed to be zero. Let u_A be the input displacement, which is nothing but the displacement of point A in the y-direction (Fig. 13a). Similarly, let u_B be the output displacement, which is again nothing but the displacement of point D in y-direction (Fig. 13a). Additionally, the rotation of the point D has been denoted as θ_D. In what follows, we shall write the force–displacement (and moment–rotation) equations for parallelogram-1 at point D (output point) and point A (input point). As the horizontal reaction at D ($F_{D'}$) does not have a significant contribution in the amplification process, it has been omitted in the calculations.

$$u_A = C^G_A(2,2) \times F_A - U_1 \times F_D - U_2 \times M_D \tag{16}$$

$$u_D = -C^G_D(2,2) \times F_D - C^G_D(2,6) \times M_D + U_1 \times F_A \tag{17}$$

$$\theta_D = -C^G_D(6,6) \times M_D + U_2 \times F_A - C^G_D(6,2) \times F_D = 0 \tag{18}$$

Here C^G_A is the compliance at point A with respect to G, and $C^G_A(2,2)$ is a compliance factor of the matrix C^G_A. C^G_D represents the compliance at the point D with respect to G. U_1 relates the y-displacement at A (i.e., u_A) due to force in the y-direction at location D (i.e., F_D). From Maxwell's reciprocal theorem, U_1 should also relate the y-displacement at D (i.e., u_D) as a result of force at A (i.e., F_A). Similarly another parameter U_2 relates M_D and u_A; therefore, it will relate F_A and θ_D as well.

The mechanism that is obtained after removing the parallelogram-1 from the full mechanism will now be considered. This mechanism will also have point D. Figure 13(b) depicts this mechanism with reactions. So once again, the force–displacement (and moment/rotation) equations at point D can be written as

https://doi.org/10.1017/S0263574722000327 Published online by Cambridge University Press

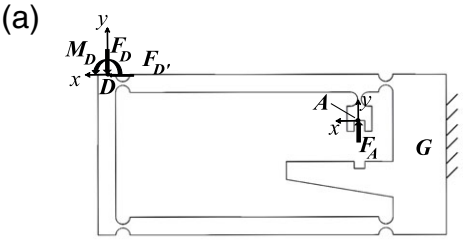

Parallelogram mechanism of limb-1 separated from the micromanipulator with input and reaction forces/moments

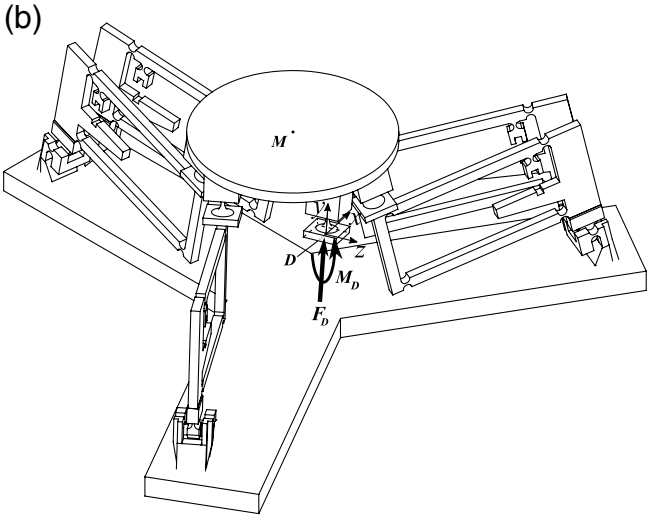

Full mechanism with parallel limbs 2-6

Figure 13. *Amplification ratio formulation.*

$$u_D = C_{D(2-6)}(2,2) \times F_D + C_{D(2-6)}(2,6) \times M_D \tag{19}$$

$$\theta_D = C_{D(2-6)}(6,6) \times M_D + C_{D(2-6)}(6,2) \times F_D = 0 \tag{20}$$

where $C_{D(2-6)}$ is the compliance of the mechanism excluding limb-1 at point D.

For the original full mechanism, if input compliance is C_{in}^G, the following expression will also be valid at point A:

$$u_A = C_{in}^G(2,2) \times F_A \tag{21}$$

We now have six force–displacement (and moment–rotation) equations (Eqs. 16−21). Eliminating F_D, F_A, M_D, U_1, and U_2 from these equations, the expression for AR in terms of the compliance values is finally obtained as

$$AR = \frac{u_D}{u_A} = \sqrt{\frac{Num}{Den}} \tag{22}$$

where,

$$\begin{aligned} Num = \Big\{ & C_A^G(2,2)\big(C_{D(2-6)}(2,2)\big)^2\big(C_{D(2-6)}(6,6)\big)^2 - 2C_A^G(2,2)\, C_{D(2-6)}(2,2)\, C_{D(2-6)}(2,6)\, C_{D(2-6)}(6,2)\, C_{D(2-6)} \\ & (6,6) + C_A^G(2,2)\left(C_{D(2-6)}(2,6)\right)^2\left(C_{D(2-6)}(6,2)\right)^2 - \left(C_{D(2-6)}(2,2)\right)^2\left(C_{D(2-6)}(6,6)\right)^2 C_{in}^G(2,2) \\ & + 2C_{D(2-6)}(2,2)\, C_{D(2-6)}(2,6)\, C_{D(2-6)}(6,2)\, C_{D(2-6)}(6,6)\, C_{in}(2,2) \\ & - \left(C_{D(2-6)}(2,6)\right)^2\left(C_{D(2-6)}(6,2)\right)^2 C_{in}(2,2)\Big\} \end{aligned}$$

https://doi.org/10.1017/S0263574722000327 Published online by Cambridge University Press

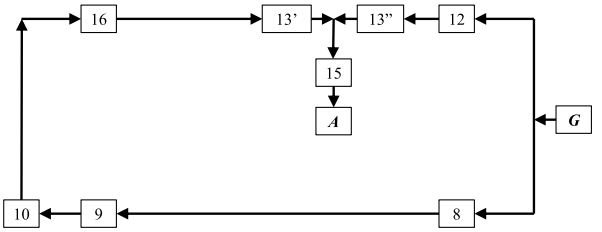

Figure 14. *Connectivity graph of members for calculation of* C_A^G.

and

$$Den = \Big\{ \left(C_{in}^G(2,2)\right)^2 \Big(C_D^G(2,2) \left(C_{D(2-6)}(6,6)\right)^2 - C_D^G(2,6)\, C_{D(2-6)}(6,2)\, C_{D(2-6)}(6,6) - C_D^G(6,2)\, C_{D(2-6)}(6,2)\, C_{D(2-6)}(6,6) + C_D^G(6,6) \left(C_{D(2-6)}(6,6)\right)^2 + C_{D(2-6)}(2,2) \left(C_{D(2-6)}(6,6)\right)^2 - C_{D(2-6)}(2,6)\, C_{D(2-6)}(6,2)\, C_{D(2-6)}(6,6) \Big) \Big\}.$$

From Eq. (22), additional information in terms of the expressions of C_A^G, C_D^G, $C_{D(2-6)}$, and C_{in} is needed. These expressions have been derived in the following sections.

4.2.1. Expression for C_A^G

With reference to Fig. 14, if we start from point G and proceed clockwise, we can observe that flexure member 8, 9, 10, 16, and 13' are in serial connection. Hence, their resultant transformed compliance at A can be given as

$$C_{A:8,9,10,16,13'}^G = T_8^A C_8 \left(T_8^A\right)^T + T_9^A C_9 \left(T_9^A\right)^T + T_{10}^A C_{10} \left(T_{10}^A\right)^T + T_{16}^A C_{16} \left(T_{16}^A\right)^T + T_{13'}^A C_{13'} \left(T_{13'}^A\right)^T \tag{23}$$

Similarly, while proceeding anticlockwise from G, we can find joint-12 and 13" to be serially connected. Their resultant transformed compliance at A is

$$C_{A:12,13''}^G = T_{12}^A C_{12} \left(T_{12}^A\right)^T + T_{13''}^A C_{13''} \left(T_{13''}^A\right)^T \tag{24}$$

The compliances $C_{A:8,9,10,16,13'}^G$ and $C_{A:12,13''}^G$ are in parallel. Moreover, these two compliances together make a serial connection with the last flexure member, flexure-15, to reach the desired point of interest which is A. The final required expression can be calculated as

$$C_A^G = \left(\left(C_{A:8,9,10,16,13'}^G\right)^{-1} + \left(C_{A:12,13''}^G\right)^{-1} \right)^{-1} + T_{15}^A C_{15} \left(T_{15}^A\right)^T \tag{25}$$

4.2.2. Expression for C_D^G

The compliance C_D^G is same as C_D^U, which has already been obtained in Section 4.1.1 (Eq. 12). The same equation is presented below for C_D^G.

$$C_D^G = \Bigg(\left(T_8^D C_8 \left(T_8^D\right)^T + T_9^D C_9 \left(T_9^D\right)^T + T_{10}^D C_{10} \left(T_{10}^D\right)^T \right)^{-1} + \Big(T_{12}^D C_{12} \left(T_{12}^D\right)^T + T_{16}^D C_{16} \left(T_{16}^D\right)^T + T_{17}^D C_{17} \left(T_{17}^D\right)^T \Big)^{-1} \Bigg)^{-1} \tag{26}$$

4.2.3. Expression for $C_{D(2-6)}$

In Section 4.1.2, the expression for output compliance of the current CPM was formulated (Eq. 15). The same equation is presented below.

https://doi.org/10.1017/S0263574722000327 Published online by Cambridge University Press

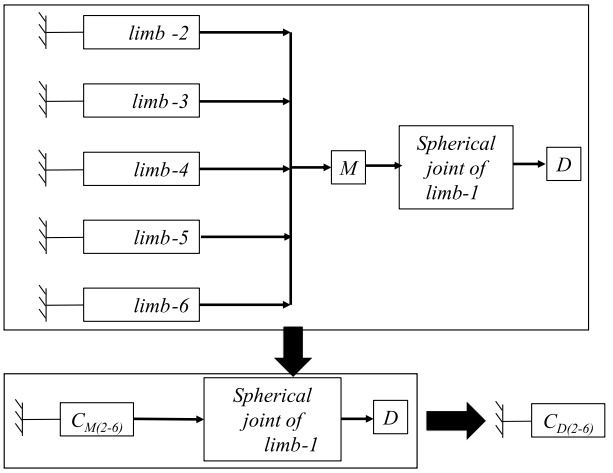

Figure 15. *Simplified connectivity graph of steps involved in calculation of* $C_{D(2-6)}$.

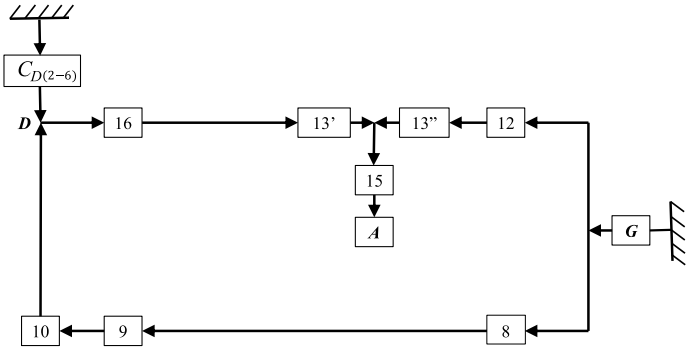

Figure 16. *Simplified connectivity graph of members for calculation of input compliance.*

$$C_M = \left(\left(T_{P1}^M C_{P1} \left(T_{P1}^M \right)^T \right)^{-1} + \left(T_{P2}^M C_{P2} \left(T_{P2}^M \right)^T \right)^{-1} + \left(T_{P3}^M C_{P3} \left(T_{P3}^M \right)^T \right)^{-1} + \left(T_{P4}^M C_{P4} \left(T_{P4}^M \right)^T \right)^{-1} + \left(T_{P5}^M C_{P5} \left(T_{P5}^M \right)^T \right)^{-1} + \left(T_{P6}^M C_{P6} \left(T_{P6}^M \right)^T \right)^{-1} \right)^{-1} \tag{27}$$

In this equation, if we remove the first term in the right-hand side, the resulting expression would be the compliance at M for the mechanism without limb-1. Let us denote this compliance as $C_{M(2-6)}$. $C_{M(2-6)}$ when connected serially with the spherical joint of limb-1 can give us the desired compliance ($C_{D(2-6)}$). Figure 15 outlines this process.

The final expression, obtained after following the steps mentioned above, is written below.

$$C_{D(2-6)} = T_M^D C_{M(2-6)} \left(T_M^D \right)^T + T_{18}^D C_{18} \left(T_{18}^D \right)^T \tag{28}$$

4.2.4. Expression for C_{in}^G

The expression for $C_{D(2-6)}$ was derived in the previous section. Connection of $C_{D(2-6)}$ with the parallelogram-1 represents the full CPM (Fig. 16). In this context, the problem of determining the input compliance is nothing but finding out the compliance of point A with respect to G.

As member 8, 9, and 10 are serially connected, their transformed compliance at A is

$$C_{A:8,9,10}^G = T_8^A C_8 \left(T_8^A \right)^T + T_9^A C_9 \left(T_9^A \right)^T + T_{10}^A C_{10} \left(T_{10}^A \right)^T \tag{29}$$

https://doi.org/10.1017/S0263574722000327 Published online by Cambridge University Press

Table I. *Dimensional and simulation parameters.*

Dimensional parameters for each limb (Fig. 7) (lengths in mm and angles in degrees)							
r=2	$b=4$	$t=1$	r_c=2	b_c=8	t_c=1	l_3=45	l_4=15
l_5=83	l_{2n}=7	l_7=2	l_8=3	l_9=13.41	l_{10}=5	l_{11}=5	r_s=4
t_s=1.5	l_{12}=4	l_{13}=5.4	l_{14}=13.52	r_r=2	b_r=4	t_r=1	α_i=12
$a=5$	$w=4$	$g=1.75$	p_l=13.5				
For complete mechanism (Fig. 9)							
		α_p=33.58		r_p=34.33		l_{15}=5	
Simulation parameters							
Element size (in limbs)		Element type		Young's modulus (E)		Poisson's ratio (ν)	
2 mm		C3D10		200 GPa		0.3	

This compliance is in parallel connection to $C_{D(2-6)}$ as shown in Fig. 16. Therefore,

$$C^G_{A:D} = \left(\left(T^A_D C_{D(2-6)} (T^A_D)^T\right)^{-1} + (C^G_{A:8,9,10})^{-1}\right)^{-1} \tag{30}$$

The rest of the process is similar to that followed in the derivation of compliance C^G_A. The expressions involved in the process are presented below.

$$C^G_{A:(D,16,13')} = C^G_{A:D} + T^A_{16} C_{16} \left(T^A_{16}\right)^T + T^A_{13'} C_{13'} \left(T^A_{13'}\right)^T \tag{31}$$

$$C^G_{A:12,13''} = T^A_{12} C_{12} \left(T^A_{12}\right)^T + T^A_{13''} C_{13''} \left(T^A_{13''}\right)^T \tag{32}$$

From Eqs. (31) and (32), the final expression can be written as

$$C^G_{in} = \left((C^G_{A:(D,16,13')})^{-1} + (C^G_{A:12,13''})^{-1}\right)^{-1} + T^A_{15} C_{15} \left(T^A_{15}\right)^T \tag{33}$$

This is the required expression for input compliance.

5. Comparison and validation of model using FEA

The analytical models for output compliance, input compliance, and AR of the CPM in consideration were obtained in the previous section. In this section, these models will be validated by FEA through Abaqus-6.14 simulations [32]. The various dimensional parameters (defined in Figs. 7 and 9) and simulation parameters for CPM are given in Table I. In the simulation, all the revolute flexures in the parallelogram linkages have been given identical dimensions.

Figure 17 represents the FEA model of the CPM prepared in Abaqus-6.14 environment. The 10 node tetrahedral element C3D10 has been used to create mesh of the CPM. As the deformations are mainly expected to be concentrated in the flexure joint locations, they have been provided with a fine mesh by setting curvature control to 0.01. A convergence analysis was done to determine the suitable mesh size. In the FEA model, a unit force in y-direction is applied at the input point (A) of the limb-1 (Fig. 18a) while keeping the link G fixed. The resulting displacements at point A (input displacement) and D (output displacement) in y-direction are observed. The input motion obtained in such a manner is nothing but the input compliance of the CPM in consideration. Whereas the ratio of the output and input displacement represents the AR. The output compliance in the FEA model can be determined by the application of a unit force/moment at the output point M of the CPM (Fig. 18b) and obtaining the corresponding displacement/rotation. Table II elaborates on the results obtained from the analytical (matrix) model and FEA simulations. Here, FEA results have been considered as the benchmark or true result for calculating the deviations.

For output and input compliance, deviations were found to be from around 7% to 11%. These errors mainly originate from the inaccuracy of expressions of the adopted compliance factors for the flexure

https://doi.org/10.1017/S0263574722000327 Published online by Cambridge University Press

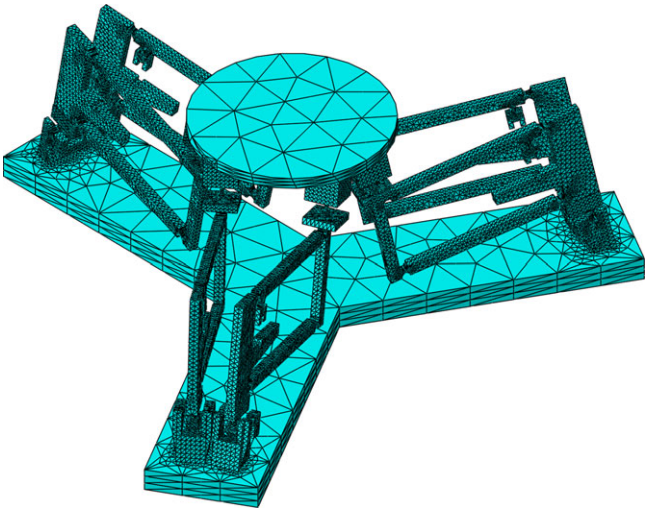

Figure 17. *FEA model of the CPM.*

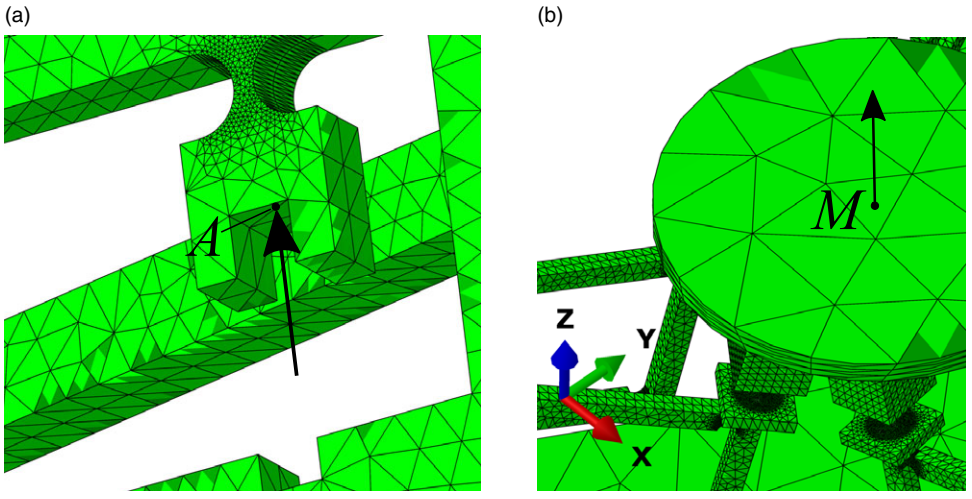

Figure 18. *Input and output compliance determination using FEA simulations.*

joints. Now let us look at the results for AR. From Eq. (22), we can observe that the derived expression for AR involves many compliance factors. Now, these factors themselves have errors ranging from 5% to 15%. This can be the reason for a high 24.3% deviation in AR result.

In order to reconcile the values closely, we assume that compliance values obtained by FEA are closer to reality than the analytical values and substitute them back into the expression for AR; it reduces the error from 24.3% to less than 15%. Finally, it can be established that the formulated expressions in Section 4 agree to the FEA results with acceptable deviations.

6. Influence of dimensional parameters on CPM's compliances and AR

In Section 4, we formulated the analytical relationships for the given CPM. With the help of those expressions, we can observe the effect of CPM dimensions on its performance. We have seen that each

https://doi.org/10.1017/S0263574722000327 Published online by Cambridge University Press

Table II. *Comparison of results obtained from analytical and FEA model.*

	Output compliance (μm/N)			Input compliance	Amplification
Model	***x*-direction**	***y*-direction**	***z*-direction**	**(μm/N)**	**ratio (AR)**
Matrix model	5.749	5.749	11.344	0.300	6.757
FEA	6.184	6.185	12.736	0.319	5.436
Deviation (%)	7.034	7.049	10.930	5.956	−24.301

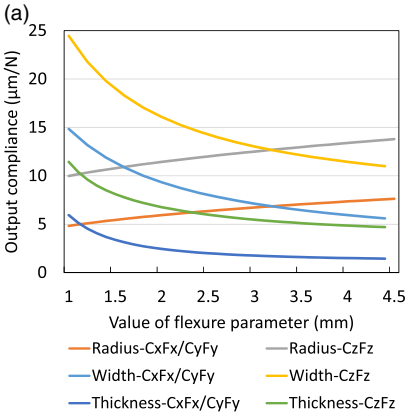

Effect of flexure parameters on output compliance.

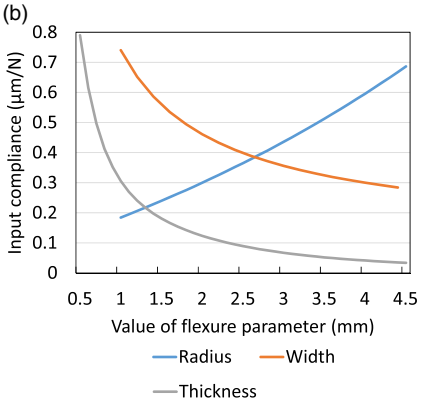

Effect of flexure parameters on input compliance.

Figure 19. *Effect of flexure dimensions on compliance.*

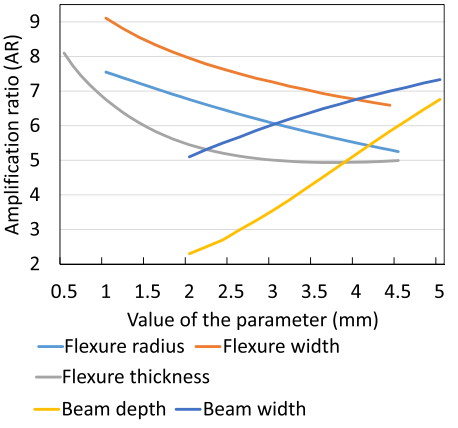

Figure 20. *Effect of flexure and beam parameters on AR.*

limb of the current design has a parallelogram mechanism. This parallelogram mechanism incorporates four revolute flexures (8, 10, 12, and 17). As stated earlier, the dimensional parameters (r_r, b_r, and t_r (Fig. 5a)) of all these flexures are the same. The effect of dimensional parameters on output compliance, input compliance, and AR has been shown in Figs. 19(a), 19(b), and 20, respectively.

6.1. Effect of dissimilarity in flexure parameter on the typical limb AR

The results in the earlier sections have shown that the performance of the CPM depends on geometrical parameters of the flexure. In general, most of the available CPMs in literature are designed with the

https://doi.org/10.1017/S0263574722000327 Published online by Cambridge University Press

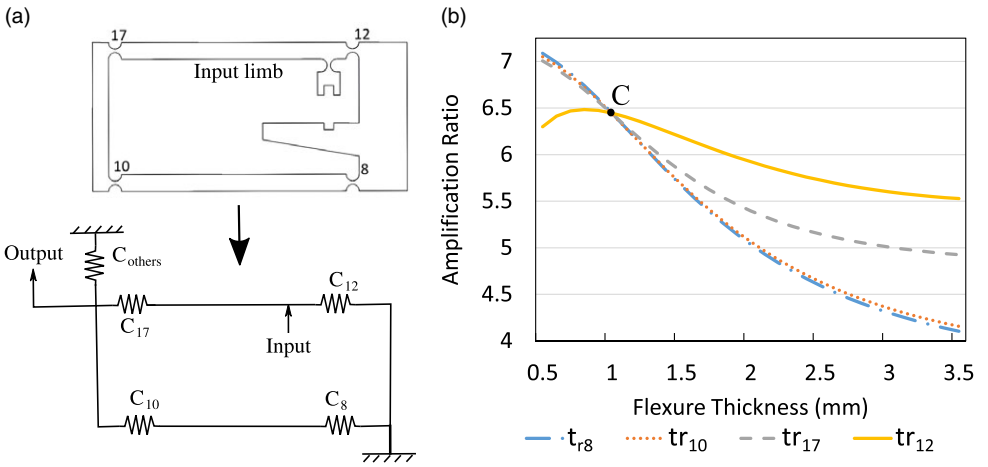

Figure 21. *Effect of dissimilar flexures.*

assumption that a particular class of flexures have similar geometrical parameters when used repeatedly. It means that, for instance, if a CPM is made up of revolute flexures, then all of them would have the same radii, thicknesses, and widths. Manufacturing tolerances and variation can cause some deviation in the AR of the linkage. Furthermore, even additional coupled effects due to any dissimilarities can affect the AR. However, at the same time, one can introduce dissimilarity to alter the spatial compliance/performance of the micromanipulator. We shall consider the limb's parallelogram mechanism (Fig. 13a) to explore this possibility in this section. In the parallelogram mechanism, the thickness of the four revolute flexures: flexure-8, 10, 12, and 17, will be changed one at a time, and its effect on the AR will be observed. Figure 21(a) represents an equivalent compliance scheme of the series–parallel chain of a typical limb shown. The input at a and the output of the link in the same plane is considered. The rest of the manipulator has an equivalent compliance C_{others} in the same plane. In this exercise, we change the compliance by adjusting thicknesses t_{r8}, t_{r10}, t_{r12}, and t_{r17} independently, as mentioned. The result of this exploration is presented in Fig. 21(a). In this figure, point C (flexure thickness $(t_r) = 1$ mm) corresponds to the original design value. Furthermore, it will be a starting point for variation in this exploration. We reduce the thickness up to 50% and increase it to around 300%. The results presented in Fig. 21(b) reveal the following:

(i) Any increase in the flexure thickness increases the stiffness and reduces the AR significantly. Whereas a reduction in flexure thickness reduces the stiffness and increases the AR by a lesser amount. Further, the closer joints (one joint away) have less effect than the farther ones (more than one joint away) in the chain.

(ii) ***Thickness of flexure-12:*** This flexure is located on the input limb, nearest to the input point. For the higher thickness values, this flexure manifests the least reduction in AR compared to other flexures. While flexure-8, 10, and 17 yield almost the same result for a decrease in thickness, that is, a surge in the AR value, flexure-12 reveals different behavior for the same range of variation. During a decrease in the thickness of flexure-12, as we start approaching point C, we observe a drop in the rate of change of AR. Just beyond point C, AR stays constant for a while, and ultimately it starts decreasing. This observation can be explained as follows. The proper working of the parallelogram mechanism for amplification requires the input limb to rotate about flexure-12. For this to happen, flexure-12 should have a certain amount of flexibility as well as strength. As per on scheme, when the thickness of flexure-12 was decreased, the rest of the flexures' thicknesses were kept constant. So, while this change does make the flexure-12 more flexible, it also renders the joint weak to resist the external load and moments applied by the rest of the

https://doi.org/10.1017/S0263574722000327 Published online by Cambridge University Press

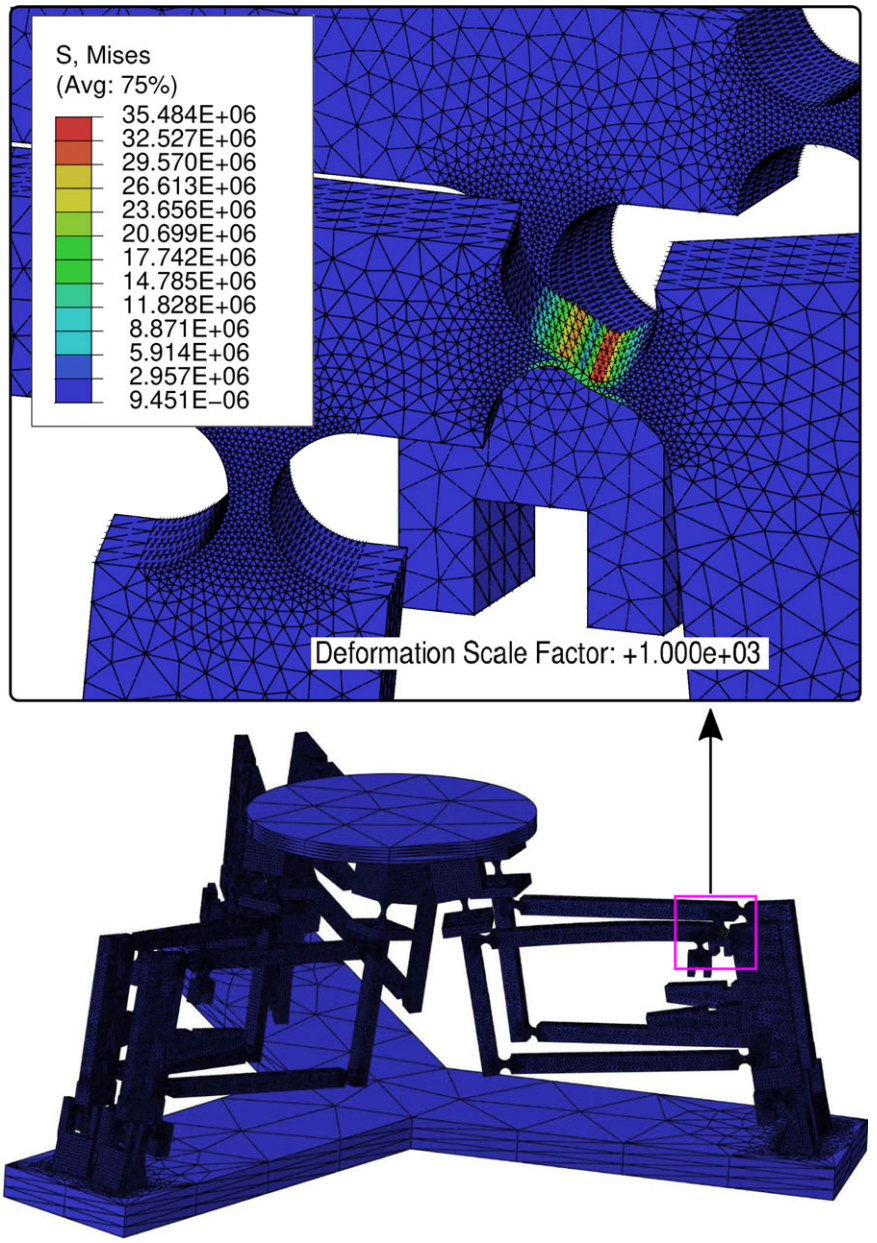

Figure 22. *Stretching of a thin flexure.*

mechanism. Therefore, beyond a limit, the decrease in thickness will only result in stretching of the joint and lead to a significant weakening of the mechanism.

Let us understand this phenomenon through an FEA simulation. We shall reconsider the FEA model of the whole CPM as done previously in Section 5. In one of the parallelogram linkages of this model, flexure-12 thickness has been reduced to 0.2 *mm*. All other dimensions are the same as before (Table I). Material, element type, and curvature control settings are also unchanged. However, the element size is kept smaller (0.5 *mm*) due to the presence of a thin flexure. We subject the parallelogram (with thin flexure) to an input force of 4 *N*. The system's response in Fig. 22 shows the flexure stretching that was predicted earlier.

https://doi.org/10.1017/S0263574722000327 Published online by Cambridge University Press

As a consequence of the joint stretching, some part of the input motion gets lost. For the reasons mentioned above, we observe a reduction in AR for flexure-12 for low thickness values in Fig. 21(b). Thus, to obtain a high AR, as a guideline, we can state that the flexure nearest to the input point should not be designed weaker than other flexures and can be used as a baseline constant.

(iii) ***Thickness of flexure-17***: As shown in Fig. 21(a), flexure-17 is on the left side of the input limb. This flexure also exhibits a reduction in AR for an increase in thickness. However, in this case, the rate of decline is more than that of flexure-12. On the other hand, if we decrease the thickness, then unlike flexure-12, we observe an increase in AR.

(iv) ***Thickness of flexure-8 and flexure-10***: Two flexures are more than one joint away from input actuation point. Flexure-8 lies on the right side of the bottom limb in the parallelogram mechanism. As we increase its thickness, it leads to a reduction in AR. Moreover, a decrease in the thickness causes growth in AR. The change in AR for flexure-8 and flexure-10 (the other flexure in the same limb) is almost coincident. It is also important to note that in the opposing parallel paths, the AR reduces very sharply by increasing the thickness of the flexure. In fact, for higher thickness values, these two flexures produce more reduction in AR than the other two remaining flexures (flexure-12 and 17).

The effect of change in thickness for each joint in the parallelogram linkage has been understood from previous discussions. Now, if the aim is to improve the AR, then to achieve that, we can fix the geometry of flexure-12 and decrease the thickness of any of the other three joints. It should be appreciated that this is, in fact, one of the many ways to improve AR. In the present case, at a time, the thickness of only one flexure was changed, the rest being the same. A more detailed study of the combined effects of the stiffness variation can give a better design choice. An optimization study can also be carried out in this context.

7. Conclusions

The compliance modeling of a full 6-DOF series–parallel flexure-based Stewart platform-like micromanipulator was presented in this article. The matrix method has been considered to carry out the mathematical modeling. The compliance matrix, which depends on the dimensions and material of the member, was utilized in the matrix method. The analytical expression for output compliance was formulated for the current design by dividing the full CPM into multiple subsystems. Furthermore, the AR relation was also obtained for the parallelogram linkage of a limb. Finally, the expression for input compliance of the CPM has been derived. The validation of the analytical model was performed using FEA in the Abaqus-6.14 environment. Simulation results revealed that analytical models have less than 15% deviations from the FEA model. Then with the help of formulated analytical models, the effect of some major dimensional parameters on the performance of the CPM was presented in various plots. In the end, it has been indicated that dissimilarity of geometrical parameters of the flexures may lead to better performance in terms of displacement amplification.

We should keep in mind that limits on output and input compliance constrain the geometry of any CPM. Furthermore, being the thinnest part of the mechanism, the flexures are most prone to material failures. There would also be upper limits on flexure sizes based on space constraints. All these factors should be considered while finalizing the flexure geometry. Such models, along with the analytical models derived in this paper, can be extremely helpful in discovering optimal configurations in future.

Conflicts of interest. The design of the micromanipulator is subject to a patent filed by the institute where the authors are carrying out their research.

Financial support. None.

https://doi.org/10.1017/S0263574722000327 Published online by Cambridge University Press

Ethical considerations. None.

Authors' contributions. None.

References

[1] L. L. Howell. *Compliant Mechanisms* (John Wiley & Sons, 2001).
[2] H. H. Pham and I. M. Chen, "Stiffness modeling of flexure parallel mechanism," *Precis. Eng.* **29**(4), 467–478 (2005).
[3] T. Hb, M. Hw, J. Xia, K. Ma and L. Zz, "Stiffness analysis of a metamorphic parallel mechanism with three configurations," *Mech. Mach. Theory* **142**(7), 103595 (2019).
[4] N. Wang, Z. Zhang and X. Zhang, "Stiffness analysis of corrugated flexure beam using stiffness matrix method," *Proc. Inst. Mech. Eng. C J. Mech. Eng. Sci.* **233**(5), 1818–1827 (2019).
[5] M. Ling, L. L. Howell, J. Cao and G. Chen, "Kinetostatic and dynamic modeling of flexure-based compliant mechanisms: A survey," *Appl. Mech. Rev.* **72**(3), 1 (2020).
[6] L. L. Howell and A. Midha, "A method for the design of compliant mechanisms with small-length flexural pivots," *J. Mech. Des.* **116**(1), 280–290 (1994).
[7] X. Tang and I. M. Chen, "A Large-displacement 3-DOF Flexure Parallel Mechanism with Decoupled Kinematics Structure," **In:** *2006 IEEE/RSJ International Conference on Intelligent Robots and Systems* (IEEE, 2006) pp. 1668–1673.
[8] Y. Li and Q. Xu, "A novel piezoactuated XY stage with parallel, decoupled, and stacked flexure structure for micro-/nanopositioning," *IEEE Trans. Ind. Electron.* **58**(8), 3601–3615 (2010).
[9] Y. Li and Z. Wu, "Design, analysis and simulation of a novel 3-DOF translational micromanipulator based on the PRB model," *Mech. Mach. Theory* **100**(9), 235–258 (2016).
[10] X. Herpe, R. Walker, M. Dunnigan and X. Kong, "On a simplified nonlinear analytical model for the characterisation and design optimisation of a compliant XY micro-motion stage," *Robot. Comput. Integr. Manuf.* **49**, 66–76 (2018).
[11] S. Xu, X. Zhu, Z. Dong and P. Liu, "Nonlinear modeling and analysis of compliant mechanisms with circular flexure hinges based on quadrature beam elements," *Proc. Inst. Mech. Eng. C J. Mech. Eng. Sci.* **233**(9), 3277–3285 (2019).
[12] Y. Li and Q. Xu, "Design and analysis of a totally decoupled flexure-based XY parallel micromanipulator," *IEEE Trans. Robot.* **25**(3), 645–657 (2009).
[13] Q. Liang, D. Zhang, Z. Chi, Q. Song, Y. Ge and Y. Ge, "Six-DOF micro-manipulator based on compliant parallel mechanism with integrated force sensor," *Robot. Comput. Integr. Manuf.* **27**(1), 124–134 (2011).
[14] A. Klimchik, A. Pashkevich and D. Chablat, "Fundamentals of manipulator stiffness modeling using matrix structural analysis," *Mech. Mach. Theory* **133**, 365–394 (2019).
[15] S. Wu, Z. Shao, H. Su and H. Fu, "An energy-based approach for kinetostatic modeling of general compliant mechanisms," *Mech. Mach. Theory* **142**(2), 103588 (2019).
[16] D. Zhang, P. Li, J. Zhang, H. Chen, K. Guo and M. Ni, "Design and assessment of a 6-DOF Micro/nanopositioning system," *IEEE/ASME Trans. Mechatron.* **24**(5), 2097–2107 (2019).
[17] A. Al-Jodah, B. Shirinzadeh, M. Ghafarian, T. K. Das and J. Pinskier, "Design, modeling, and control of a large range 3-DOF micropositioning stage," *Mech. Mach. Theory* **156**(1), 104159 (2021).
[18] F. Chen, W. Dong, M. Yang, L. Sun and Z. Du, "A PZT actuated 6-DOF positioning system for space optics alignment," *IEEE/ASME Trans. Mechatron.* **24**(6), 2827–2838 (2019).
[19] S. Kang, M. G. Lee and Y. M. Choi, "Six degrees-of-freedom direct-driven nanopositioning stage using crab-leg flexures," *IEEE/ASME Trans. Mechatron.* **25**(2), 513–525 (2020).
[20] F. Chen, Q. Zhang, Y. Gao and W. Dong, "A review on the flexure-based displacement amplification mechanisms," *IEEE Access* **8**, 205919–205937 (2020).
[21] N. Lobontiu, J. Hunter, J. Keefe and J. Westenskow, "Tripod mechanisms with novel spatial Cartesian flexible hinges," *Mech. Mach. Theory* **167**(8), 104521 (2022).
[22] M. Ling, D. Song, X. Zhang, X. He, H. Li, M. Wu, et al., "Analysis and design of spatial compliant mechanisms using a 3-D dynamic stiffness model," *Mech. Mach. Theory* **168**(7), 104581 (2022).
[23] S. K. Mishra and C. S. Kumar, "Design and Kinematics of a Compliant Stewart Micromanipulator," **In:** *2018 International Conference on Manipulation, Automation and Robotics at Small Scales (MARSS)* (IEEE, 2018) pp. 1–6.
[24] J. M. Paros and L. Weisbord, "How to design flexure hinges," *Mach. Des.* **37**, 151–156 (1965).
[25] N. Lobontiu. *Compliant Mechanisms: Design of Flexure Hinges* (CRC Press, 2002).
[26] S. T. Smith. *Flexures: Elements of Elastic Mechanisms* (CRC Press, 2014).
[27] D. Stewart, "A platform with six degrees of freedom," *Proc. Inst. Mech. Eng.* **180**(1), 371–386 (1965).
[28] V. E. Gough, "Universal Tyre Test Machine," **In:** *Proceedings of the FISITA 9th International Technical Congress*, (London, 1962) pp. 117–137.
[29] Y. K. Yong and T. F. Lu, "Kinetostatic modeling of 3-RRR compliant micro-motion stages with flexure hinges," *Mech. Mach. Theory* **44**(6), 1156–1175 (2009).
[30] Y. Li, J. Huang and H. Tang, "A compliant parallel XY micromotion stage with complete kinematic decoupling," *IEEE Trans. Autom. Sci. Eng.* **9**(3), 538–553 (2012).
[31] Maple 18 User Manual, Waterloo Maple (Maplesoft) (2014).
[32] Abaqus 6.14 Documentation, Dassault Systemes Simulia Corporation (2014).
[33] Y. Koseki, T. Tanikawa, N. Koyachi and T. Arai, "Kinematic analysis of a translational 3-dof micro-parallel mechanism using the matrix method," *Adv. Robot.* **16**(3), 251–264 (2002).

https://doi.org/10.1017/S0263574722000327 Published online by Cambridge University Press

A. Compliance matrices of flexures

1. Compliance matrix for revolute flexures with geometry (r_r, b_r, t_r) [33]:

$$C_r = \begin{bmatrix} c_5 & 0 & 0 & 0 & 0 & 0 \\ 0 & c_1 & 0 & 0 & 0 & c_3 \\ 0 & 0 & c_2 & 0 & -c_4 & 0 \\ 0 & 0 & 0 & c_8 & 0 & 0 \\ 0 & 0 & -c_4 & 0 & c_6 & 0 \\ 0 & c_3 & 0 & 0 & 0 & c_7 \end{bmatrix} \tag{A1}$$

where, $c_1 = \frac{9\pi r_r^{5/2}}{2Eb_r t_r^{5/2}} + \frac{3\pi r_r^{3/2}}{2Eb_r t_r^{5/2}}$; $c_2 = \frac{12\pi r_r^2}{Eb_r^3}(\sqrt{\frac{r_r}{t_r}} - \frac{1}{4})$; $c_3 = \frac{9}{2}\frac{\pi r_r^{3/2}}{Eb_r t_r^{5/2}}$;
$c_4 = \frac{12 r_r}{Eb_r^3}(\pi\sqrt{\frac{r_r}{t_r}} - 1 - \frac{\pi}{2})$; $c_5 = \frac{1}{Eb_r}(\pi\sqrt{\frac{r_r}{t_r}} - \frac{\pi}{2})$; $c_6 = 12\frac{1}{Eb_r^3}(\pi\sqrt{\frac{r_r}{t_r}} - 1 - \frac{\pi}{2})$;
$c_7 = \frac{9}{2}\frac{\pi\sqrt{r_r}}{Eb_r t_r^{5/2}}$; $c_8 = \frac{9}{4}\frac{\pi\sqrt{r_r}}{Gb_r t_r^{5/2}}$; $G = \frac{E}{2(1+\nu)}$.

2. Compliance matrix for connecting links (modelled as Euler-Bernoulli beams) with geometry (depth-a, width-w, length-l) [33]:

$$C_b = \begin{bmatrix} b_5 & 0 & 0 & 0 & 0 & 0 \\ 0 & b_1 & 0 & 0 & 0 & b_3 \\ 0 & 0 & b_2 & 0 & -b_4 & 0 \\ 0 & 0 & 0 & b_8 & 0 & 0 \\ 0 & 0 & -b_4 & 0 & b_6 & 0 \\ 0 & b_3 & 0 & 0 & 0 & b_7 \end{bmatrix} \tag{A2}$$

where, $b_l = \dfrac{4l^3}{Ea^3w}$; $b_2 = \dfrac{6l^2}{Ea^3w}$; $b_3 = \dfrac{4l^3}{Eaw^3}$; $b_4 = \dfrac{6l^2}{Eaw^3}$; $b_5 = \dfrac{l}{Eaw}$; $b_6 = \dfrac{12l}{Eaw^3}$; $b_7 = \dfrac{12l}{Ea^3w}$; $b_8 = \dfrac{10l}{Ga^3w}$.

3. Compliance matrix for spherical flexure with geometry ($r_s = 4$ mm, $t_s = 1.5$ mm):

$$C_s = \begin{bmatrix} s_5 & 0 & 0 & 0 & 0 & 0 \\ 0 & s_1 & 0 & 0 & 0 & s_3 \\ 0 & 0 & s_1 & 0 & -s_4 & 0 \\ 0 & 0 & 0 & s_8 & 0 & 0 \\ 0 & 0 & -s_4 & 0 & s_6 & 0 \\ 0 & s_3 & 0 & 0 & 0 & s_6 \end{bmatrix} \tag{A3}$$

where, $s_5 = 10.490 \times 10^{-6}$ mm/N; $s_1 = 875.000 \times 10^{-6}$ mm/N; $s_3 = s_4 = 199.000 \times 10^{-6}$ mm/N-mm; $s_6 = 49.760 \times 10^{-6}$ rad/N-mm; $s_8 = 63.930 \times 10^{-6}$ rad/N-mm. For the current design of the compliant spherical flexure, errors in the the analytical relations (from [25]) were very high. Moreover, any other accurate formulation could not be found in the literature for the concerned flexure. Therefore, for this flexure, values of compliance factors (presented above) has been taken from FEA simulations.

https://doi.org/10.1017/S0263574722000327 Published online by Cambridge University Press

B. Transformation matrices

$$T_2^u = \begin{bmatrix} 1 & 0 & 0 & 0 & b/2+g+r_c+t_c/2 & -l_{2n}-r_c \\ 0 & 1 & 0 & -b/2-g-r_c-t_c/2 & 0 & -r \\ 0 & 0 & 1 & l_{2n}+r_c & r & 0 \\ 0 & 0 & 0 & 1 & 0 & 0 \\ 0 & 0 & 0 & 0 & 1 & 0 \\ 0 & 0 & 0 & 0 & 0 & 1 \end{bmatrix} \tag{B1}$$

$$T_4^u = \begin{bmatrix} 1 & 0 & 0 & 0 & -b/2-g-r_c-t_c/2 & -l_{2n}-r_c \\ 0 & 1 & 0 & b/2+g+r_c+t_c/2 & 0 & -r \\ 0 & 0 & 1 & l_{2n}+r_c & r & 0 \\ 0 & 0 & 0 & 1 & 0 & 0 \\ 0 & 0 & 0 & 0 & 1 & 0 \\ 0 & 0 & 0 & 0 & 0 & 1 \end{bmatrix} \tag{B2}$$

$$T_6^u = \begin{bmatrix} 0 & 0 & -1 & 0 & l_{2n} & 0 \\ 0 & 0 & 0 & 0 & 0 & 0 \\ 0 & -1 & 0 & 0 & 0 & -l_{2n} \\ 0 & 0 & 0 & 0 & 0 & -1 \\ 0 & 0 & 0 & 0 & 0 & 0 \\ 0 & 0 & 0 & 0 & -1 & 0 \end{bmatrix} \tag{B3}$$

$$T_8^D = \begin{bmatrix} 1 & 0 & 0 & 0 & 0 & -l_6+r_r+t_r/2 \\ 0 & 1 & 0 & 0 & 0 & l_{11}/2+l_5-2\,r_r \\ 0 & 0 & 1 & l_6-r_r-t_r/2 & -l_{11}/2-l_5+2\,r_r & 0 \\ 0 & 0 & 0 & 1 & 0 & 0 \\ 0 & 0 & 0 & 0 & 1 & 0 \\ 0 & 0 & 0 & 0 & 0 & 1 \end{bmatrix} \tag{B4}$$

$$T_9^D = \begin{bmatrix} 1 & 0 & 0 & 0 & 0 & -l_6+r_r+t_r/2 \\ 0 & 1 & 0 & 0 & 0 & l_{11}/2+2\,r_r \\ 0 & 0 & 1 & l_6-r_r-t_r/2 & -l_{11}/2-2\,r_r & 0 \\ 0 & 0 & 0 & 1 & 0 & 0 \\ 0 & 0 & 0 & 0 & 1 & 0 \\ 0 & 0 & 0 & 0 & 0 & 1 \end{bmatrix} \tag{B5}$$

$$T_{10}^D = \begin{bmatrix} 1 & 0 & 0 & 0 & 0 & -l_6+r_r+t_r/2 \\ 0 & 1 & 0 & 0 & 0 & l_{11}/2 \\ 0 & 0 & 1 & l_6-r_r-t_r/2 & -l_{11}/2 & 0 \\ 0 & 0 & 0 & 1 & 0 & 0 \\ 0 & 0 & 0 & 0 & 1 & 0 \\ 0 & 0 & 0 & 0 & 0 & 1 \end{bmatrix} \tag{B6}$$

https://doi.org/10.1017/S0263574722000327 Published online by Cambridge University Press

$$T_{12}^{D}=\begin{bmatrix}1&0&0&0&0&-l_{10}/2\\0&1&0&0&0&l_{11}/2+l_5-2\,r_r\\0&0&1&l_{10}/2&-l_{11}/2-l_5+2\,r_r&0\\0&0&0&1&0&0\\0&0&0&0&1&0\\0&0&0&0&0&1\end{bmatrix} \tag{B7}$$

$$T_{16}^{D}=\begin{bmatrix}1&0&0&0&0&-l_{10}/2\\0&1&0&0&0&l_{11}/2+2\,r_r\\0&0&1&l_{10}/2&-l_{11}/2-2\,r_r&0\\0&0&0&1&0&0\\0&0&0&0&1&0\\0&0&0&0&0&1\end{bmatrix} \tag{B8}$$

$$T_{17}^{D}=\begin{bmatrix}1&0&0&0&0&-l_{10}/2\\0&1&0&0&0&l_{11}/2\\0&0&1&l_{10}/2&-l_{11}/2&0\\0&0&0&1&0&0\\0&0&0&0&1&0\\0&0&0&0&0&1\end{bmatrix} \tag{B9}$$

$$T_{19}^{P}=\begin{bmatrix}0&-1&0&0&0&-l_9\\1&0&0&0&0&0\\0&0&1&0&-l_9&0\\0&0&0&-1&0&0\\0&0&0&1&0&0\\0&0&0&0&0&1\end{bmatrix} \tag{B10}$$

$$T_{u}^{P1}=\begin{bmatrix}1&0&0&0&0&-(l_9+2\,r_s+l_8+l_7+l_3)\\0&1&0&0&0&(l_{11}/2+l_5+l_4/2)\\0&0&1&(l_9+2\,r_s+l_8+l_7+l_3)&-(l_{11}/2+l_5+l_4/2)&0\\0&0&0&1&0&0\\0&0&0&0&1&0\\0&0&0&0&0&1\end{bmatrix} \tag{B11}$$

$$T_{D}^{P1}=\begin{bmatrix}1&0&0&0&0&-(l_9+2\,r_s+l_8+l_7+l_3)\\0&1&0&0&0&0\\0&0&1&(l_9+2\,r_s+l_8+l_7+l_3)&0&0\\0&0&0&1&0&0\\0&0&0&0&1&0\\0&0&0&0&0&1\end{bmatrix} \tag{B12}$$

https://doi.org/10.1017/S0263574722000327 Published online by Cambridge University Press

$$T_{Pi}^{M} = \begin{bmatrix} R_{Pi}^{M} & S(r_{Pi}^{M})R_{Pi}^{M} \\ 0 & R_{Pi}^{M} \end{bmatrix} \tag{B13}$$

where,

$$R_{Pi}^{M} = \begin{bmatrix} \cos(\psi_i)\cos(\theta_i) & \cos(\psi_i)\sin(\theta_i)\sin(\phi_i) - \sin(\psi_i)\cos(\phi_i) & \cos(\psi_i)\sin(\theta_i)\cos(\phi_i) + \sin(\psi_i)\sin(\phi_i) \\ \sin(\psi_i)\cos(\theta_i) & \sin(\psi_i)\sin(\theta_i)\sin(\phi_i) + \cos(\psi_i)\cos(\phi_i) & \sin(\psi_i)\sin(\theta_i)\cos(\phi_i) - \cos(\psi_i)\sin(\phi_i) \\ -\sin(\theta_i) & \cos(\theta_i)\sin(\phi_i) & \cos(\theta_i)\cos(\phi_i) \end{bmatrix}$$

where i varies from 1 to 6 for all limbs. Angles (in degrees) for the corresponding rotation matrices are as follows: $\psi_1 = 187.825, \theta_1 = 12, \phi_1 = 90$; $\psi_2 = 172.175, \theta_2 = 12, \phi_2 = 90$; $\psi_3 = 307.875, \theta_3 = 12, \phi_3 = 90$; $\psi_4 = 292.175, \theta_4 = 12, \phi_4 = 90$; $\psi_5 = 67.825, \theta_5 = 12, \phi_5 = 90$;$\psi_6 = 52.175, \theta_6 = 12, \phi_6 = 90$.

Also,
$$S_{P1}^{M} = \begin{bmatrix} 0 & l_{14} & -r_p \sin\left(\frac{\pi(60-\alpha_p/2)}{180}\right) \\ -l_{14} & 0 & -r_p \cos\left(\frac{\pi(60-\alpha_p/2)}{180}\right) \\ r_p \sin\left(\frac{\pi(60-\alpha_p/2)}{180}\right) & r_p \cos\left(\frac{\pi(60-\alpha_p/2)}{180}\right) & 0 \end{bmatrix};$$

$$S_{P2}^{M} = \begin{bmatrix} 0 & l_{14} & -r_p \sin\left(\frac{\pi(60+\alpha_p/2)}{180}\right) \\ -l_{14} & 0 & -r_p \cos\left(\frac{\pi(60+\alpha_p/2)}{180}\right) \\ r_p \sin\left(\frac{\pi(60+\alpha_p/2)}{180}\right) & r_p \cos\left(\frac{\pi(60+\alpha_p/2)}{180}\right) & 0 \end{bmatrix};$$

$$S_{P3}^{M} = \begin{bmatrix} 0 & l_{14} & r_p \sin\left(\frac{\pi(60+\alpha_p/2)}{180}\right) \\ -l_{14} & 0 & -r_p \cos\left(\frac{\pi(60+\alpha_p/2)}{180}\right) \\ -r_p \sin\left(\frac{\pi(60+\alpha_p/2)}{180}\right) & r_p \cos\left(\frac{\pi(60+\alpha_p/2)}{180}\right) & 0 \end{bmatrix};$$

$$S_{P4}^{M} = \begin{bmatrix} 0 & l_{14} & r_p \sin\left(\frac{\pi(60-\alpha_p/2)}{180}\right) \\ -l_{14} & 0 & -r_p \cos\left(\frac{\pi(60-\alpha_p/2)}{180}\right) \\ -r_p \sin\left(\frac{\pi(60-\alpha_p/2)}{180}\right) & r_p \cos\left(\frac{\pi(60-\alpha_p/2)}{180}\right) & 0 \end{bmatrix};$$

$$S_{P5}^{M} = \begin{bmatrix} 0 & l_{14} & -r_p \sin\left(\frac{\pi\alpha_p}{360}\right) \\ -l_{14} & 0 & r_p \cos\left(\frac{\pi\alpha_p}{360}\right) \\ r_p \sin\left(\frac{\pi\alpha_p}{360}\right) & -r_p \cos\left(\frac{\pi\alpha_p}{360}\right) & 0 \end{bmatrix};$$

$$S_{P6}^{M} = \begin{bmatrix} 0 & l_{14} & r_p \sin\left(\frac{\pi ap}{360}\right) \\ -l_{14} & 0 & r_p \cos\left(\frac{\pi\alpha_p}{360}\right) \\ -r_p \sin\left(\frac{\pi\alpha_p}{360}\right) & -r_p \cos\left(\frac{\pi\alpha_p}{360}\right) & 0 \end{bmatrix}.$$

$$T_{8}^{A} = \begin{bmatrix} 1 & 0 & 0 & 0 & 0 & -l_{14} - p_l - l_{10}/2 \\ 0 & 1 & 0 & 0 & 0 & l_{13} \\ 0 & 0 & 1 & l_{14} + p_l + l_{10}/2 & -l_{13} & 0 \\ 0 & 0 & 0 & 1 & 0 & 0 \\ 0 & 0 & 0 & 0 & 1 & 0 \\ 0 & 0 & 0 & 0 & 0 & 1 \end{bmatrix} \tag{B14}$$

https://doi.org/10.1017/S0263574722000327 Published online by Cambridge University Press

$$T_9^A = \begin{bmatrix} 1 & 0 & 0 & 0 & 0 & -l_{14} - p_l - l_{10}/2 \\ 0 & 1 & 0 & 0 & 0 & -l_5 + 4\,r_r + l_{13} \\ 0 & 0 & 1 & l_{14} + p_l + l_{10}/2 & l_5 - 4\,r_r - l_{13} & 0 \\ 0 & 0 & 0 & 1 & 0 & 0 \\ 0 & 0 & 0 & 0 & 1 & 0 \\ 0 & 0 & 0 & 0 & 0 & 1 \end{bmatrix} \tag{B15}$$

$$T_{10}^A = \begin{bmatrix} 1 & 0 & 0 & 0 & 0 & -l_{14} - p_l - l_{10}/2 \\ 0 & 1 & 0 & 0 & 0 & -l_5 + 2\,r_r + l_{13} \\ 0 & 0 & 1 & l_{14} + p_l + l_{10}/2 & l_5 - 2\,r_r - l_{13} & 0 \\ 0 & 0 & 0 & 1 & 0 & 0 \\ 0 & 0 & 0 & 0 & 1 & 0 \\ 0 & 0 & 0 & 0 & 0 & 1 \end{bmatrix} \tag{B16}$$

$$T_{16}^A = \begin{bmatrix} -1 & 0 & 0 & 0 & 0 & -l_{12} - 2\,r_r - l_{10}/2 \\ 0 & 1 & 0 & 0 & 0 & -l_5 + 4\,r_r + l_{13} \\ 0 & 0 & -1 & l_{12} + 2\,r_r + l_{10}/2 & l_5 - 4\,r_r - l_{13} & 0 \\ 0 & 0 & 0 & -1 & 0 & 0 \\ 0 & 0 & 0 & 0 & 1 & 0 \\ 0 & 0 & 0 & 0 & 0 & -1 \end{bmatrix} \tag{B17}$$

$$T_{13'}^A = \begin{bmatrix} -1 & 0 & 0 & 0 & 0 & -l_{12} - 2\,r_r - l_{10}/2 \\ 0 & 1 & 0 & 0 & 0 & 0 \\ 0 & 0 & -1 & l_{12} + 2\,r_r + l_{10}/2 & 0 & 0 \\ 0 & 0 & 0 & -1 & 0 & 0 \\ 0 & 0 & 0 & 0 & 1 & 0 \\ 0 & 0 & 0 & 0 & 0 & -1 \end{bmatrix} \tag{B18}$$

$$T_{13''}^A = \begin{bmatrix} 1 & 0 & 0 & 0 & 0 & l_{12} + 2\,rr + l_{10}/2 \\ 0 & 1 & 0 & 0 & 0 & 0 \\ 0 & 0 & 1 & -l_{12} - 2\,r_r - l_{10}/2 & 0 & 0 \\ 0 & 0 & 0 & 1 & 0 & 0 \\ 0 & 0 & 0 & 0 & 1 & 0 \\ 0 & 0 & 0 & 0 & 0 & 1 \end{bmatrix} \tag{B19}$$

$$T_{12}^A = \begin{bmatrix} 1 & 0 & 0 & 0 & 0 & l_{12} + 2\,r_r + l_{10}/2 \\ 0 & 1 & 0 & 0 & 0 & l_{13} \\ 0 & 0 & 1 & -l_{12} - 2\,r_r - l_{10}/2 & -l_{13} & 0 \\ 0 & 0 & 0 & 1 & 0 & 0 \\ 0 & 0 & 0 & 0 & 1 & 0 \\ 0 & 0 & 0 & 0 & 0 & 1 \end{bmatrix} \tag{B20}$$

https://doi.org/10.1017/S0263574722000327 Published online by Cambridge University Press

$$T_{15}^{A} = \begin{bmatrix} 0 & 1 & 0 & 0 & 0 & l_{12} + 2\,r_r \\ -1 & 0 & 0 & 0 & 0 & 0 \\ 0 & 0 & 1 & 0 & -l_{12} - 2\,r_r & 0 \\ 0 & 0 & 0 & 0 & 1 & 0 \\ 0 & 0 & 0 & -1 & 0 & 0 \\ 0 & 0 & 0 & 0 & 0 & 1 \end{bmatrix} \tag{B21}$$

$$T_{D}^{A} = \begin{bmatrix} 1 & 0 & 0 & 0 & 0 & l_{12} + 2\,r_r + l_{10} \\ 0 & 1 & 0 & 0 & 0 & -l_5 + 2\,r_r + l_{13} - l_{11}/2 \\ 0 & 0 & 1 & -l_{12} - 2\,r_r - l_{10} & l_5 - 2\,r_r - l_{13} + l_{11}/2 & 0 \\ 0 & 0 & 0 & 1 & 0 & 0 \\ 0 & 0 & 0 & 0 & 1 & 0 \\ 0 & 0 & 0 & 0 & 0 & 1 \end{bmatrix} \tag{B22}$$

$$T_{M}^{D} = \begin{bmatrix} R_M^D & S(r_M^D)R_M^D \\ 0 & R_M^D \end{bmatrix} \tag{B23}$$

where, $R_M^D = (R_{P1}^M)^{-1}$;
and

$$S(r_M^D) = \begin{bmatrix} 0 & -K_1 \sin\left(\frac{\pi\ (60 - \alpha_p/2)}{180}\right) & K_2 + \frac{l_{14}}{\cos(\pi/15)} + r_p - \frac{l_{14}}{\sin(\pi/15)} \\ K_1 \sin\left(\frac{\pi\ (60 - \alpha_p/2)}{180}\right) & 0 & -K_1 \sin\left(\frac{\pi\ (60 - \alpha_p/2)}{180}\right) \\ -K_2 - \frac{l_{14}}{\cos(\pi/15)} - r_p + \frac{l_{14}}{\sin(\pi/15)} & K_1 \sin\left(\frac{\pi\ (60 - \alpha_p/2)}{180}\right) & 0 \end{bmatrix}$$

Again, where, $K_1 = r_p + (l_9 + 2\,r_s + l_8 + l_7) \sin\left(\frac{\pi}{15}\right)$; $K_2 = l_7 + l_8 + 2\,r_s + l_9$.

Cite this article: S. K. Mishra and C. S. Kumar (2022). "Compliance modeling of a full 6-DOF series–parallel flexure-based Stewart platform-like micromanipulator", Robotica **40**, 3435–3462. https://doi.org/10.1017/S0263574722000327